Article

Neuron

Homeostatic Plasticity Shapes Cell-Type-Specific Wiring in the Retina

Highlights

- Optogenetics and pharmacogenetics show B6 cells provide dominant input to ONα-RGCs
- Removing B6 cells from developing circuits triggers cell-type-specific rewiring
- Cell-type-specific rewiring precisely restores light responses of ONα-RGCs
- Homeostatic plasticity shapes cell-type-specific connectivity in the retina

Authors

Nai-Wen Tien, Florentina Soto, Daniel Kerschensteiner

Correspondence

kerschensteinerd@wustl.edu

In Brief

Tien et al. discover circuit-level homeostatic plasticity in the retina. After removal of their dominant bipolar cell input, ONα retinal ganglion cells adjust connectivity with other bipolar cells in cell-type-specific ratios to precisely preserve their light responses.

Tien et al., 2017, Neuron *94*, 656–665
May 3, 2017
http://dx.doi.org/10.1016/j.neuron.2017.04.016

CellPress

CellPress

Neuron
Article

Homeostatic Plasticity Shapes Cell-Type-Specific Wiring in the Retina

Nai-Wen Tien,[1,2] Florentina Soto,[1] and Daniel Kerschensteiner[1,3,4,5,6,*]
[1]Department of Ophthalmology and Visual Sciences
[2]Graduate Program in Neuroscience
[3]Department of Neuroscience
[4]Department of Biomedical Engineering
[5]Hope Center for Neurological Disorders
Washington University School of Medicine, St. Louis, MO 63110, USA
[6]Lead Contact
*Correspondence: kerschensteinerd@wustl.edu
http://dx.doi.org/10.1016/j.neuron.2017.04.016

SUMMARY

Convergent input from different presynaptic partners shapes the responses of postsynaptic neurons. Whether developing postsynaptic neurons establish connections with each presynaptic partner independently or balance inputs to attain specific responses is unclear. Retinal ganglion cells (RGCs) receive convergent input from bipolar cell types with different contrast responses and temporal tuning. Here, using optogenetic activation and pharmacogenetic silencing, we found that type 6 bipolar (B6) cells dominate excitatory input to ONα-RGCs. We generated mice in which B6 cells were selectively removed from developing circuits (*B6-DTA*). In *B6-DTA* mice, ONα-RGCs adjusted connectivity with other bipolar cells in a cell-type-specific manner. They recruited new partners, increased synapses with some existing partners, and maintained constant input from others. Patch-clamp recordings revealed that anatomical rewiring precisely preserved contrast and temporal frequency response functions of ONα-RGCs, indicating that homeostatic plasticity shapes cell-type-specific wiring in the developing retina to stabilize visual information sent to the brain.

INTRODUCTION

To extract specific information, postsynaptic neurons combine input from different presynaptic cell types in precise ratios. During development, molecular interactions between pre- and postsynaptic partners set up initial connectivity patterns, which are subsequently refined (Sanes and Yamagata, 2009; Williams et al., 2010; Yogev and Shen, 2014). Refinement occurs at many levels, from the molecular composition and the architecture of individual synapses (Turrigiano and Nelson, 2004; Wefelmeyer et al., 2016), to the formation of new synapses and elimination of existing ones (Morgan et al., 2011; Purves and Lichtman, 1980), to the large-scale organization of neuronal projections and cell numbers (Antonini and Stryker, 1993; Riccomagno and Kolodkin, 2015; Yu et al., 2004). Remarkably, refinement balances changes across all levels to stabilize activity in emerging circuits (i.e., homeostatic plasticity). The importance of homeostatic plasticity to circuit development is underscored by recent evidence for its failures in many neurodevelopmental disorders (Ebert and Greenberg, 2013; Ramocki and Zoghbi, 2008; Turrigiano and Nelson, 2004). Homeostatic plasticity is known to mediate interactions between pre- and postsynaptic partners that maintain constant average firing rates of neurons by controlling synaptic scaling (Davis and Müller, 2015; Hengen et al., 2013; Pozo and Goda, 2010). Whether homeostatic plasticity also mediates interactions between different presynaptic inputs and adjusts patterns of convergent innervation (i.e., circuit-level plasticity) to stabilize specific computations of postsynaptic neurons is unknown.

In the mammalian retina, approximately 15 types of bipolar cells relay photoreceptor signals from the outer to the inner plexiform layer (IPL) (Euler et al., 2014; Shekhar et al., 2016). Bipolar cell types differ in their contrast responses and in their temporal filtering of photoreceptor signals (Baden et al., 2013; Borghuis et al., 2013; Euler et al., 2014; Franke et al., 2017; Ichinose et al., 2014). In the IPL, bipolar cell types converge in specific ratios onto the dendrites of 30–40 retinal ganglion cell (RGC) types (Calkins and Sterling, 2007; Dunn and Wong, 2014; Helmstaedter et al., 2013), which inherit the contrast responses and temporal tuning of their combined inputs (Baden et al., 2016; Murphy and Rieke, 2006). The relationship of bipolar cell innervation and light responses has been characterized particularly well for ONα-RGCs. Compared to other RGCs, ONα-RGCs encode contrast linearly and with high sensitivity (Murphy and Rieke, 2006; Zaghloul et al., 2003). Anatomical circuit reconstructions suggest that ONα-RGCs are innervated by several bipolar cell types, with B6 cells accounting for approximately 70% of excitatory synapses on their dendrites (Morgan et al., 2011; Schwartz et al., 2012). The responses of ONα-RGCs are accurately predicted by their excitatory input (Grimes et al., 2014; Murphy and Rieke, 2006; Zaghloul et al., 2003), and a receptive field model based on type 6 bipolar (B6) cell innervation alone captures many response features (Schwartz et al., 2012). However, whether B6 cells provide functional input to ONα-RGCs has not been directly tested, and whether during development ONα-RGCs

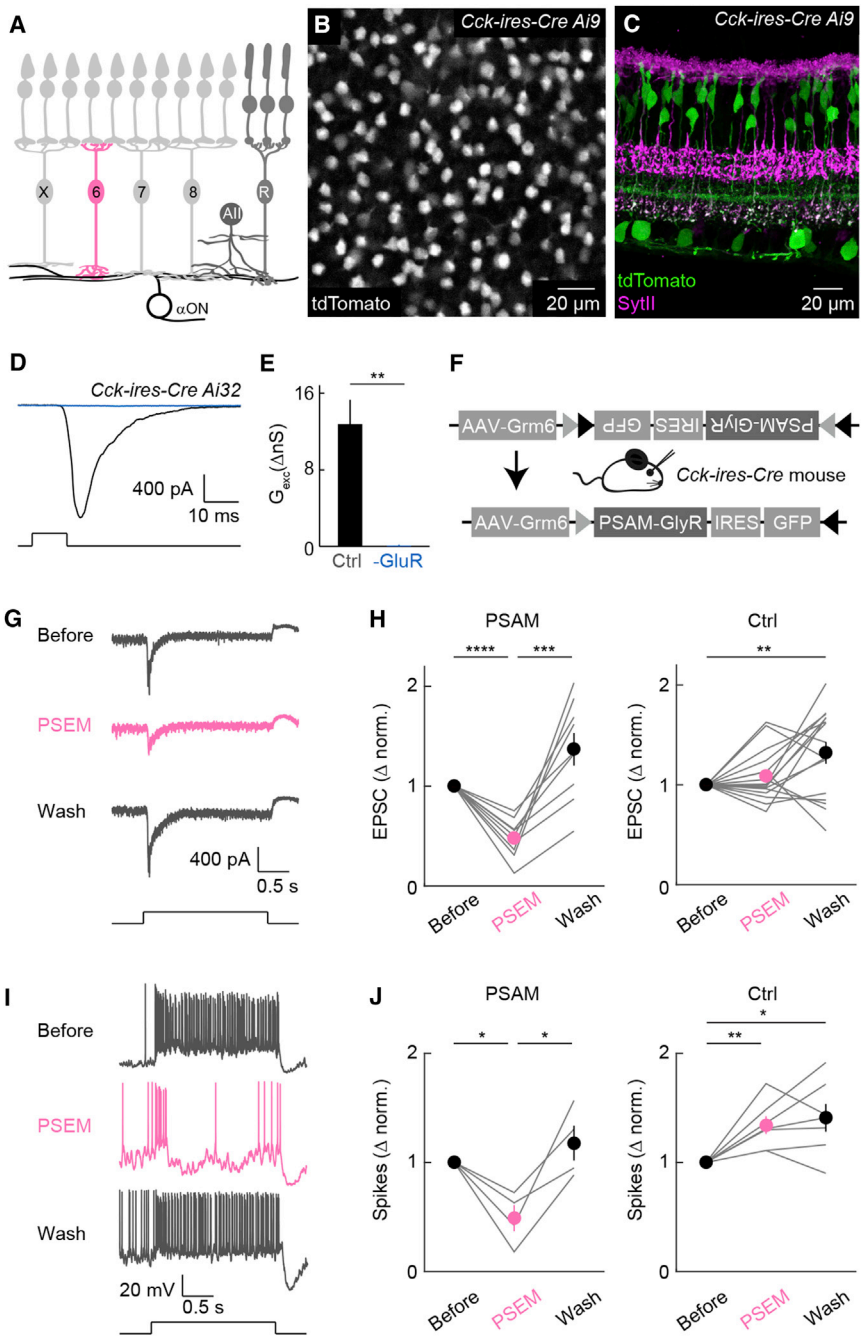

Figure 1. B6 Cells Provide Dominant Excitatory Input to ONα-RGCs

(A) Schematic illustrating converging bipolar cell input to ONα-RGCs. X, 6, 7, and 8 refer to cone bipolar cell types (Euler et al., 2014), whereas R indicates RBCs, which in wild-type mice provide mostly indirect input via AII amacrine cells (*AII*) and cone bipolar cells to ONα-RGCs.

(B) Distribution of tdTomato-expressing cells in the inner nuclear layer of a P21 whole-mount *Cck-ires-Cre Ai9* retina.

(C) Vibratome section of a P21*Cck-ires-Cre Ai9* retina showing tdTomato expression in some amacrine cells, RGCs, and B6 cells. The latter is confirmed by immunostaining of synaptotagmin II (*SytII*), an axonal marker of B2 and B6 cells.

(D and E) Representative EPSC traces (D) and summary data of excitatory conductances (E) of ONα-RGCs elicited by optogenetic stimulation of B6 cells in the absence (black) or presence (blue) of AMPA and NMDA receptor antagonists (Ctrl, 12.81 ± 2.54 nS; −*GluR*:, 0.08 ± 0.11 nS; n = 8, p = 0.002). L-AP4, ACET, and hexamethonium were included in the bath all the time.

(F) Schematic of the AAV virus injected for pharmacogenetic silencing experiments.

(G and I) Representative EPSC traces (G) and spike responses (I) of ONα-RGCs in *AAV-Grm6$_S$-PSAM^{con}* injected retinas before (Before), during (PSEM), and after (Wash) the addition of PSEM^{308}.

(H and J) Summary data of excitatory conductances (H) and spike responses (J) of ONα-RGCs with (PSAM) or without (Ctrl) *AAV-Grm6$_S$-PSAM^{con}* injection before (Before), during (PSEM), and after (Wash) the addition of PSEM^{308}. Circles (error bar) indicate mean (±SEM) of respective population. In (H), PSAM, PSEM 0.479 ± 0.064 (mean ± SEM); Wash 1.370 ± 0.163; Before versus PSEM, p = 4 *10^{-5}; PSEM versus Wash, p = 5 *10^{-4}; Before versus Wash, p = 0.053. In (H), control, PSEM 1.088 ± 0.064; Wash 1.321 ± 0.108; Before versus PSEM, p = 0.19; PSEM versus Wash, p = 0.068; Before versus Wash, p = 0.009. In (J), PSAM, PSEM 0.489 ± 0.121; Wash 1.177 ± 0.160; Before versus PSEM, p = 0.02; PSEM versus Wash, p = 0.03; Before versus Wash, p = 0.349. In (J), control, PSEM 1.343 ± 0.081; Wash 1.409 ± 0.127; Before versus PSEM, p = 0.006; PSEM versus Wash, p = 0.53; Before versus Wash, p = 0.02.

form connections with converging bipolar cells independently or balance inputs to attain specific responses is unclear.

Here, using optogenetic activation and acute pharmacogenetic silencing, we found that in wild-type mice ONα-RGC responses rely on excitatory input from B6 cells. We generated mice in which B6 cells were selectively removed from developing circuits by transgenic expression of diphtheria toxin. Anatomical circuit reconstructions and patch-clamp recordings revealed that B6 cell removal elicited circuit-level plasticity in which other bipolar cell types took over innervation in specific ratios that precisely conserved contrast responses and temporal tuning of excitatory inputs and spiking of ONα-RGCs.

RESULTS

B6 Cells Provide Dominant Excitatory Input to ONα-RGCs

ONα-RGCs receive convergent input from several bipolar cell types (Figure 1A). Although anatomical studies suggested that B6 cells account for approximately 70% of excitatory

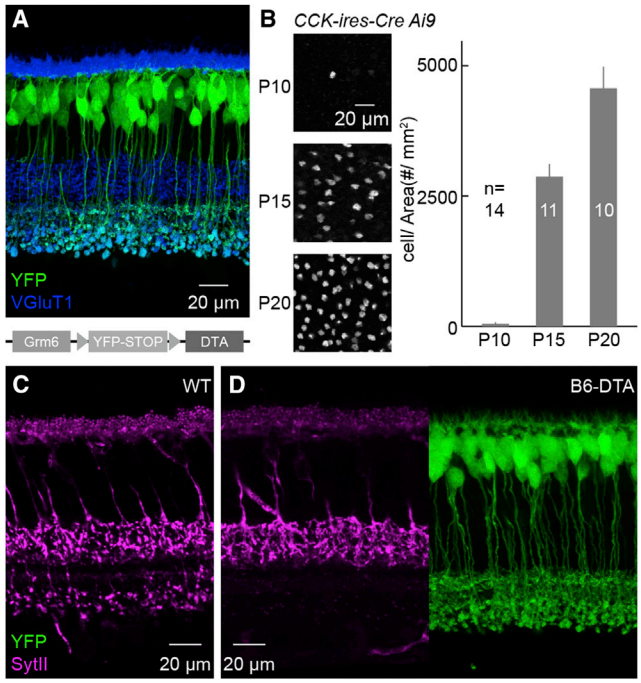

Figure 2. An Intersectional Strategy to Remove B6 Cells from the Developing Retina

(A) Representative image of a retinal section showing YFP expression in a *Grm6$_L$-YFP-DTA^{con}* mouse retina without Cre-recombination. Schematic at the bottom illustrates the genetic construct used to generate *Grm6$_L$-YFP-DTA^{con}* mice.

(B) Representative images (left) and summary data (right) for the time course of tdTomato expression in *CCK-ires-Cre Ai9* mice. P10, 48.5 ± 30.5 #/mm^2 (mean ± SEM); P15, 2,872.2 ± 245.6 #/mm^2; P20, 4,569.3 ± 411.9 #/mm^2.

(C and D) Vertical sections of wild-type (C) and *B6-DTA* (D) retinas stained for SytII and, in (D), YFP. SytII and YFP signals from the same section are shown side by side in (D).

synapses on ONα-RGC dendrites (Morgan et al., 2011; Schwartz et al., 2012), the functional input from B6 cells to ONα-RGCs has not yet been explored. To gain genetic access to B6 cells, we screened a set of Cre driver lines (Taniguchi et al., 2011) by crossing to a fluorescent reporter strain (*Ai9*, tdTomato) (Madisen et al., 2010). In *CCK-ires-Cre Ai9* mice, which were previously shown to label several RGC and amacrine cell types (Tien et al., 2015; Zhu et al., 2014), tdTomato expression in the bipolar cell layer was restricted to a single cell type. The somata of these cells were arranged in a mosaic (Figures 1B and S1); their axon terminals stratified in the ON sublamina of the IPL and stained for synaptotagmin II (SytII) (Figure 1C) (Fox and Sanes, 2007). This identifies the bipolar cells labeled in *Cck-ires-Cre Ai9* mice as B6 cells, consistent with a recent gene expression profiling study, which revealed Cck as a specific marker of B6 cells (Shekhar et al., 2016).

To test for functional connectivity of B6 cells with ONα-RGCs, we crossed *Cck-ires-Cre* mice to a strain in which channelrhodopsin-2 is expressed wherever Cre-mediated recombination occurs (*Ai32*) (Madisen et al., 2012). With photoreceptor input to bipolar cells blocked by application of L-AP4 and ACET, and cholinergic transmission blocked by inclusion of hexamethonium, optogenetic stimulation of B6 cells elicited large excitatory postsynaptic currents (EPSCs) in ONα-RGCs (Figures 1D and 1E). These currents were sensitive to AMPA and NMDA receptor antagonists, demonstrating that B6 cells provide glutamatergic input to ONα-RGCs.

To probe the contributions of B6 input to photoreceptor-mediated light responses of ONα-RGCs, we generated adeno-associated viruses (AAVs) that drive expression of the pharmacogenetic silencer PSAM$^{L141F,\ Y115F}$-GlyR-IRES-GFP (Magnus et al., 2011), PSAM for short, from promoter elements of the metabotropic glutamate receptor 6 (*Grm6$_S$*) (Lagali et al., 2008), conditioned upon Cre-mediated recombination (*AAV-Grm6$_S$-PSAM^{con}*; Figure 1F). Because *Grm6$_S$* sequences promote transcription only in ON bipolar cells (Lagali et al., 2008), their intersection with *CCK-ires-Cre* should restrict expression to B6 cells. We generated *AAV-Grm6$_S$-GFP^{con}* by removing PSAM-IRES sequences from *AAV-Grm6$_S$-PSAM^{con}*, to improve visualization of GFP. After injection of *AAV-Grm6$_S$-GFP^{con}* intravitreally in *CCK-IRES-Cre Ai9* mice, GFP expression was restricted to the bipolar cell layer, and nearly all GFP-positive cells (99%) were also tdTomato positive (Figure S2). This confirmed the cell-type specificity of our intersectional strategy. Next, we injected *AAV-Grm6$_S$-PSAM^{con}* in *CCK-ires-Cre* mice. In retinas of these mice, application of the exogenous ligand PSEM^{308} greatly reduced light-evoked EPSCs (Figures 1G and 1H) and spike responses of ONα-RGCs (Figures 1I and 1J). By contrast, without *AAV-Grm6$_S$-PSAM^{con}* injections, PSEM^{308} had no significant effect on EPSCs of ONα-RGCs (Figure 1H) and slightly enhanced their spike responses (Figure 1J). EPSCs and firing rates of ONα-RGCs were increased upon washout of PSEM^{308} irrespective of PSAM expression, likely due to off-target effects of the agonist (Figures 1H and 1J). Given that AAVs infected only a subset of B6 cells (Figure S2), the strong pharmacogenetic suppression of EPSCs, together with previous anatomical studies (Morgan et al., 2011; Schwartz et al., 2012) and results from optogenetics, suggests that B6 cells dominate excitatory input to and are required for normal light responses of ONα-RGCs.

We next measured excitatory input to ONα-RGCs during brief (250 ms) steps of varying contrast in a 300-µm diameter spot centered on the recorded cell. In addition to reducing the amplitude of tonic and stimulus-evoked EPSCs, application of PSEM^{308} in *AAV-Grm6$_S$-PSAM^{con}*-injected mice resulted in less inwardly rectified excitatory contrast response functions (Figure S2), indicating that the functional properties of B6 input differ from those of non-B6 inputs to ONα-RGCs.

An Intersectional Transgenic Strategy to Remove B6 Cells from the Developing Retina

To probe interactions of converging bipolar cell types during ONα-RGC innervation, we next wanted to selectively remove B6 cells from the developing retina. We devised an intersectional strategy similar to that used for pharmacogenetic silencing of B6 cells (Figure 1F) and crossed mice that conditionally express an attenuated version of diphtheria toxin in ON bipolar cells (*Grm6$_L$-YFP-DTA^{con}*; Figure 2A) (Morgan et al., 2011) to *CCK-ires-Cre* mice. We refer to double transgenic offspring from these

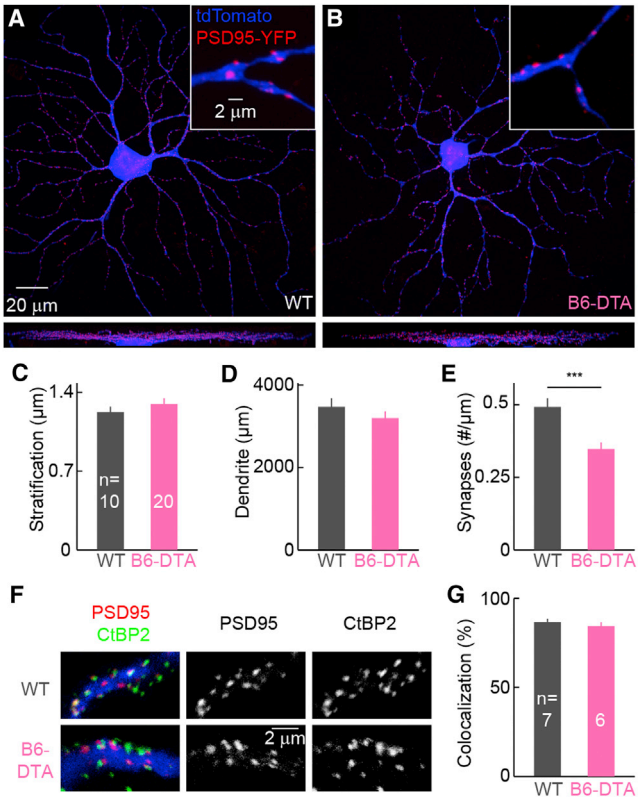

Figure 3. Effects of B6 Cell Removal on ONα-RGC Dendrites and Synapses

(A and B) Top-down (top) and side (bottom) views of ONα-RGCs biolistically labeled with cytosolic tdTomato and PSD95-YFP in wild-type (A) and *B6-DTA* (B) retinas. Insets show enlarged views of PSD95-YFP puncta along ONα-RGC dendrites.

(C–E) Summary data (mean ± SEM) of dendritic parameters of ONα-RGCs in wild-type (WT) (gray) and *B6-DTA* (pink) mice. In (C), WT, 1.22 ± 0.05 μm; *B6-DTA*, 1.29 ± 0.05 μm; p = 0.17. In (D), WT, 3,471 ± 206 μm; *B6-DTA*, 3,195 ± 166 μm; p = 0.31. In (E), WT, 0.492 ± 0.03 synapses/μm; *B6-DTA*, 0.347 ± 0.02 synapses/μm; p < 0.001.

(F and G) Representative images (F) and summary data (G) showing the co-localization of PSD95-YFP puncta with CtBP2 in wild-type (top row) and *B6-DTA* (bottom row) ONα-RGCs. In (G), WT, 86.7% ± 1.9%; B6-DTA, 84.4% ± 2.2%; p = 0.44.

crosses as *B6-DTA* mice from here on. To estimate the time course of DTA expression in these mice, we first counted tdTomato-expressing bipolar cells in *CCK-ires-Cre Ai9* mice at different ages. The number of these cells increased dramatically from postnatal day 10 (P10) to P15 (Figure 2B). Because *Ai9* can express tdTomato in the retina at least from birth on (data not shown), this time course likely reflects the rise of Cre in B6 cells. By comparison, yellow fluorescent protein (YFP) in *Grm6$_L$-YFP-DTA^{con}* and other fluorescent proteins in other *Grm6$_L$* transgenics become detectable between P3 and P7 (Kerschensteiner et al., 2009; Morgan et al., 2006, 2011). Thus, the onset of DTA expression in *B6-DTA* mice appears to be limited by Cre expression and falls between P10 and P15.

To evaluate the extent and specificity of B6 cell removal in *B6-DTA* mice, we stained sections and flat mounts of P20 retinas for SytII. In wild-type retinas, SytII labeled B2 and B6 axons in the ON and OFF sublamina of the IPL, respectively. In *B6-DTA* mice, SytII staining in the ON sublamina was lost, but staining in the OFF sublamina was unchanged (Figures 2C and 2D). In addition, YFP expression in non-B6 ON bipolar cell types was unaffected in *B6-DTA* mice. We quantified these observations in retinal flat mounts (Figure S3), confirming that >95% of B6 cells are removed from *B6-DTA* retinas by P21. Moreover, the reduction in the density of all ON bipolar cells in *B6-DTA* mice matched the density of B6 cells in wild-type mice (Figures 2B and S3F). Approximately half of the B6 cells in *B6-DTA* retinas were deleted by P15 (Figure S3), indicating that the time course of cell removal closely matched that of Cre expression. Together, these results show that B6 cells are removed selectively and nearly completely from *B6-DTA* retinas during the period of bipolar cell-RGC synaptogenesis (Fisher, 1979; Morgan et al., 2008, 2011).

Effects of B6 Cell Removal on ONα-RGC Dendrites and Synapses

To begin to analyze effects of B6 cell removal on ONα-RGCs, we biolistically labeled these cells with cytosolic tdTomato and postsynaptic density protein 95 fused to YFP (PSD95-YFP), a marker of excitatory synapses (Kerschensteiner et al., 2009; Morgan et al., 2011). We found that stratification and length of ONα-RGC dendrites were indistinguishable between *B6-DTA* mice and wild-type littermates (Figures 3A–3D). The density of PSD95-YFP puncta on ONα-RGC dendrites was reduced in *B6-DTA* mice (Figure 3E), but only by 30%, much less than the fraction of synapses (70%) contributed by B6 cells in wild-type mice (Morgan et al., 2011; Schwartz et al., 2012). This suggests that either many PSD95-YFP puncta in *B6-DTA* mice are not apposed by presynaptic release sites (i.e., orphan postsynapses), or that other bipolar cells take over ONα-RGC innervation from B6 cells. To distinguish between these possibilities, we stained retinas with biolistically labeled ONα-RGCs for CtBP2, a component of presynaptic ribbons in bipolar cells (Schmitz et al., 2000) (Figure 3F). An identical fraction (85%) of PSD95-YFP puncta on ONα-RGC dendrites co-localized with CtBP2 in *B6-DTA* mice and wild-type littermates (Figure 3G), indicating that in the absence of B6 cells other bipolar cells increase their connectivity with ONα-RGCs.

Cell-Type-Specific Rewiring of Cone Bipolar Cells with ONα-RGCs in *B6-DTA* Mice

Dendrites of ONα-RGCs overlap with axons of several ON cone bipolar cells types (B6, B7, B8, and XBC) (Dunn and Wong, 2014; Helmstaedter et al., 2013; Morgan et al., 2011). We wanted to test which of these replace input from B6 cells in *B6-DTA* mice, and whether rewiring occurs by uniform upregulation of connectivity or is cell-type specific. We sparsely labeled ON bipolar cells by intravitreal injection of a virus expressing tdTomato under control of *Grm6$_S$* (*AAV-Grm6$_S$-tdTomato*; Figure 4A) and biolistically labeled ONα-RGCs and bipolar cell-RGC synapses with cytosolic YFP and PSD95-CFP, respectively. This allowed us to analyze the connectivity of pairs of individual bipolar cells and ONα-RGCs.

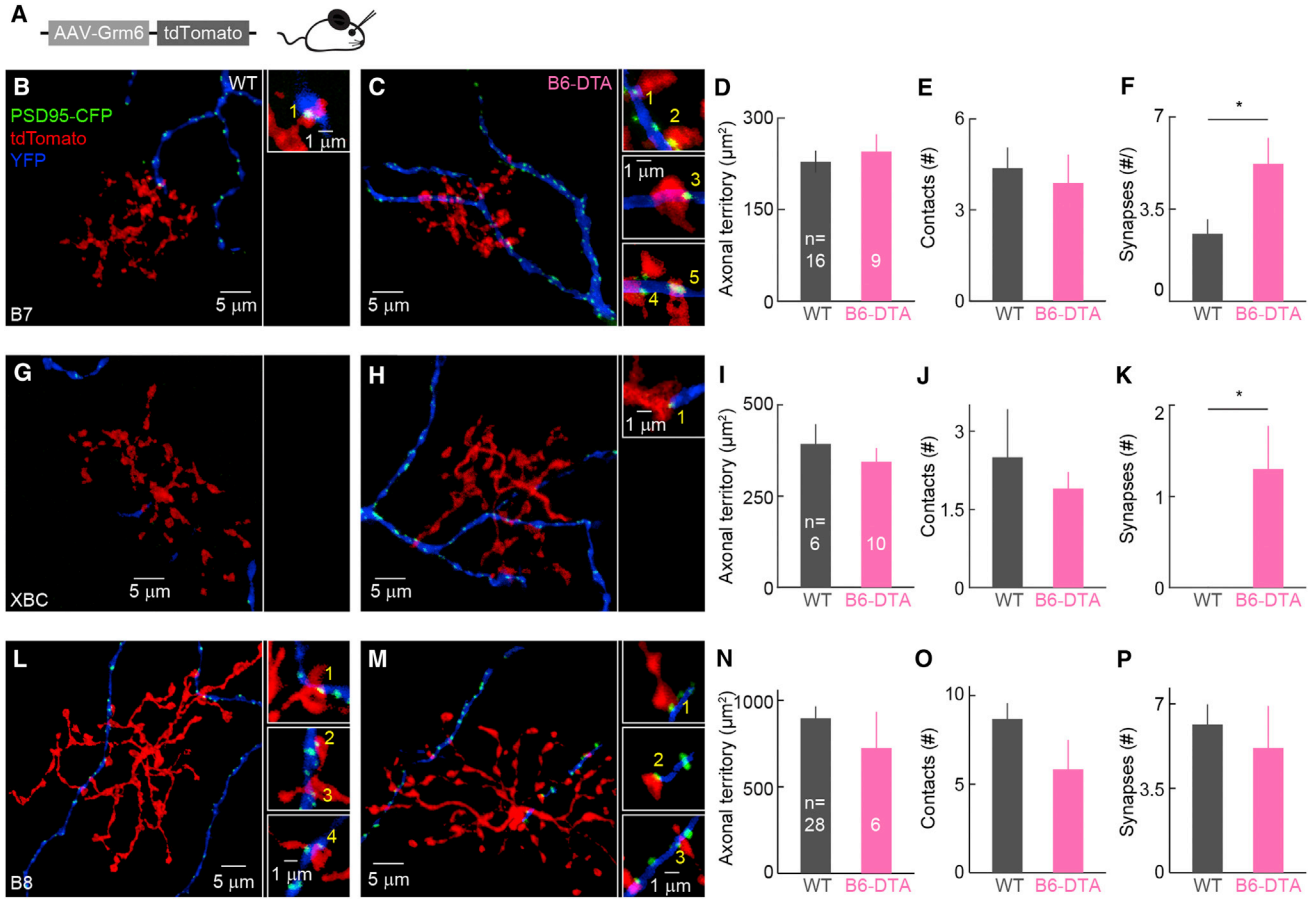

Figure 4. Cell-Type-Specific Rewiring of Cone Bipolar Cells with ONα-RGCs Following B6 Cell Removal

(A) Schematic of *AAV-Grm6*$_S$*-tdTomato* injection to sparsely label ON bipolar cells.

(B and C) Examples of isolated B7-ONα-RGC pairs in wild-type (B) and *B6-DTA* (C) retinas. Maximum intensity projections of confocal image stacks are shown on the left. The panels on the right show single planes from the image stacks at contact points between B7 cell axons (red) and ONα-RGC dendrites (blue). Synapses were identified by PSD95 puncta (green).

(D–F) Summary data for axon territories (D), axo-dendritic contacts (E), and synapse numbers (F) for B7-ONα-RGC pairs in wild-type (WT) (gray) and *B6-DTA* (pink) retinas. In (D), WT, 229 ± 18 µm^2 (mean ± SEM); *B6-DTA*, 245 ± 28 µm^2; p = 0.63. In (E), WT, 4.38 ± 0.68; *B6-DTA*, 3.89 ± 0.93; p = 0.68. In (F), WT, 2.56 ± 0.56; *B6-DTA*, 5.22 ± 0.98; p < 0.05.

(G–K) Analogous to (B) and (C) and (D)–(F) (G and H and I–K, respectively) but for XBC-ONα-RGC pairs. In (I), WT, 393 ± 54 µm^2; *B6-DTA*, 344 ± 38 µm^2; p = 0.47. In (J), WT, 2.50 ± 0.92; *B6-DTA*, 1.90 ± 0.31; p = 0.56. In (K), WT, 0.00 ± 0.00; *B6-DTA*, 1.30 ± 0.47; p = 0.02.

(L–P) Analogous to (B) and (C) and (D)–(F) (L and M and N–P, respectively) but for B8-ONα-RGC pairs. In (N), WT, 897 ± 210 µm^2; *B6-DTA*, 724 ± 210 µm^2; p = 0.47. In (O), WT, 8.68 ± 0.9; *B6-DTA*, 5.83 ± 1.66; p = 0.17. In (P), WT, 6.14 ± 0.84; *B6-DTA*, 5.17 ± 1.74; p = 0.63.

We distinguished bipolar cell types by their characteristic dendritic and axonal morphologies (Dunn and Wong, 2012; Helmstaedter et al., 2013; Morgan et al., 2011; Wässle et al., 2009). B7 cells were previously characterized as a minor input to ONα-RGCs (Morgan et al., 2011; Schwartz et al., 2012). We confirmed these observations in wild-type mice and found that in *B6-DTA* retinas, B7 cells more than doubled the number of connections with ONα-RGCs (Figures 4B, 4C, and 4F). This was accomplished without changes in the axon territories of B7 cells (Figure 4D) or the number of contacts between B7 axons and ONα-RGC dendrites (Figure 4E), by conversion of a larger fraction of contacts to synapses (i.e., connectivity fraction). In wild-type mice, axons of XBC cells occasionally touched dendrites of ONα-RGCs, but none of these contacts bore synapses (Figures 4G, 4J, and 4K). In *B6-DTA* mice, XBC axon size and contact numbers with ONα-RGCs did not change, but nearly all contacts contained synapses (Figures 4H–4K). However, bipolar cell connectivity was not uniformly upregulated in *B6-DTA* mice, as the large axons of B8 cells, which formed a significant number of synapses with ONα-RGCs in wild-type mice, were unchanged in their morphology and connectivity (Figures 4L–4P). Thus, B6 cell removal from developing circuits triggers cell-type-specific rewiring of cone bipolar cells with ONα-RGCs, which elevates a minor input to become the major one (B7), recruits a novel input type (XBC), and leaves unaltered the connections of another (B8). Rewiring is accomplished by selective changes in the connectivity fraction of bipolar cell axons without

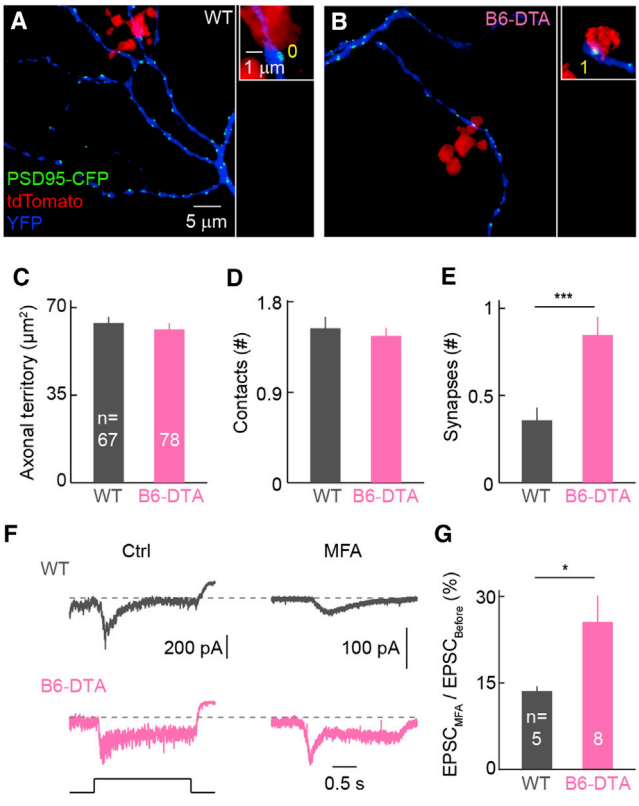

Figure 5. Increase in Connectivity between RBCs and ONα-RGCs in *B6-DTA* Mice

(A and B) Examples of isolated RBC-ONα-RGC pairs in wild-type (A) and *B6-DTA* (B) retinas. Maximum intensity projections of confocal image stacks are shown on the left. The panels on the right show single planes from the image stacks at contact points between RBC axons (red) and ONα-RGC dendrites (blue).

(C–E) Summary data of axon territories (C), axo-dendritic contacts (D), and synapses (E) for RBC-ONα-RGC pairs in wild-type (gray) and *B6-DTA* (pink) retinas. In (C), WT, 63.9 ± 2.5 µm^2; *B6-DTA*, 61.30 ± 2.36 µm^2; p = 0.46. In (D), WT, 1.54 ± 0.11; *B6-DTA*, 1.46 ± 0.08; p = 0.58. In (E), WT, 0.36 ± 0.07; *B6-DTA*, 0.85 ± 0.11; p = 2 * 10^{-4}.

(F and G) Representative EPSC traces (F) and summary data (G) of ONα-RGC responses to dim light steps (3 rhodopsin isomerizations/rod/s or R*) in the absence (left, Ctrl) or presence (right, MFA) of MFA. In (G), WT, 13.6% ± 0.8%; *B6-DTA*, 25.6% ± 4.5%; p = 0.03.

changes to their morphology or the frequency of contacts between bipolar cell axons and ONα-RGC dendrites.

Increased Direct Input from Rod Bipolar Cells to ONα-RGCs in *B6-DTA* Mice

In wild-type mice, rod bipolar cells (RBCs) provide input to ONα-RGCs—and other RGCs—predominantly by an indirect path: RBC axons form excitatory synapses with AII amacrine cells, which are electrically coupled to ON cone bipolar cells, which convey signals to ONα-RGCs (Bloomfield and Dacheux, 2001; Demb and Singer, 2015). During development, RBCs initially form synapses with ONα-RGC dendrites, but subsequently eliminate most of their connections as B6 cells increase connectivity with ONα-RGCs (Morgan et al., 2011). We wondered whether RBCs retain synapses with ONα-RGCs in *B6-DTA* mice, in which B6 cells are removed during development. We sparsely labeled RBCs by *AAV-Grm6$_S$-tdTomato* injections, and ONα-RGCs and excitatory synapses by biolistics. Similar to our observations for cone bipolar cells, we found that axon territories and the number of contacts with ONα-RGC dendrites did not change for RBCs in *B6-DTA* mice (Figures 5A–5D). However, the probability of synaptic connections more than doubled (Figure 5E), suggesting that RBCs retain synapses with ONα-RGCs when B6 cells are removed.

Indirect input from RBCs to ONα-RGCs depends on gap junctions between AII amacrine cells and ON cone bipolar cells, whereas direct synaptic input does not. In patch-clamp recordings from ONα-RGCs, we found that a larger fraction of excitatory input elicited by stimuli that predominantly recruit the RBC pathway (Murphy and Rieke, 2006) was resistant to the gap junction blocker meclofenamic acid (MFA) in *B6-DTA* mice compared to wild-type littermates (Figures 5F and 5G). This shows that anatomical rewiring mediates changes in functional connectivity in *B6-DTA* mice, which involve both cone and RBCs.

Bipolar Cell Rewiring Precisely Preserved Light Responses of ONα-RGCs in *B6-DTA* Mice

Our pairwise analysis revealed cell-type-specific changes in the connectivity of bipolar cells with ONα-RGCs in *B6-DTA* mice (Figures 4 and 5). We hypothesized that ONα-RGCs recruit bipolar cell types in specific ratios (Figure S4) (see STAR Methods) to best replace the input from B6 cells and to preserve their characteristic light responses. To test this hypothesis, we analyzed light responses of ONα-RGCs using patch-clamp recordings. In stark contrast to acute pharmacogenetic silencing of B6 cells (Figures 1G–1J), the amplitudes of excitatory inputs and spike responses of ONα-RGCs were not significantly different between *B6-DTA* mice and wild-type littermates (Figures 6A–6H). This was true both for stimuli preferentially activating rods (Figures 6A, 6B, 6D, and 6E) and for stimuli preferentially activating cones (Figures 6G, 6H, 6J, and 6K). Moreover, the characteristic contrast response functions of ONα-RGC EPSCs and spiking (Murphy and Rieke, 2006; Zaghloul et al., 2003) were precisely preserved in *B6-DTA* mice in dim (Figures 6C and 6F) and bright light conditions (Figures 6I and 6L).

In addition to contrast responses, the temporal tuning of RGCs is determined by combined input from different bipolar cell types with unique response kinetics (Baden et al., 2013; Borghuis et al., 2013; Franke et al., 2017; Ichinose et al., 2014). Measuring EPSCs during white noise stimulation, we found that the temporal tuning of bipolar cell input to ONα-RGCs was indistinguishable between *B6-DTA* mice and wild-type littermates (Figures 7A–7D).

Although our results clearly showed that presynaptic rewiring contributed to the preservation of ONα-RGCs' light responses, it was unclear whether postsynaptic scaling also played a role in this homeostasis (Pozo and Goda, 2010; Turrigiano, 2008). To address this question, we recorded spontaneous EPSCs (sEPSCs) from ONα-RGCs in wild-type and *B6-DTA* retinas. Recordings were performed in conditions that lowered the probability of vesicle fusion (i.e., zero extracellular calcium) to reduce

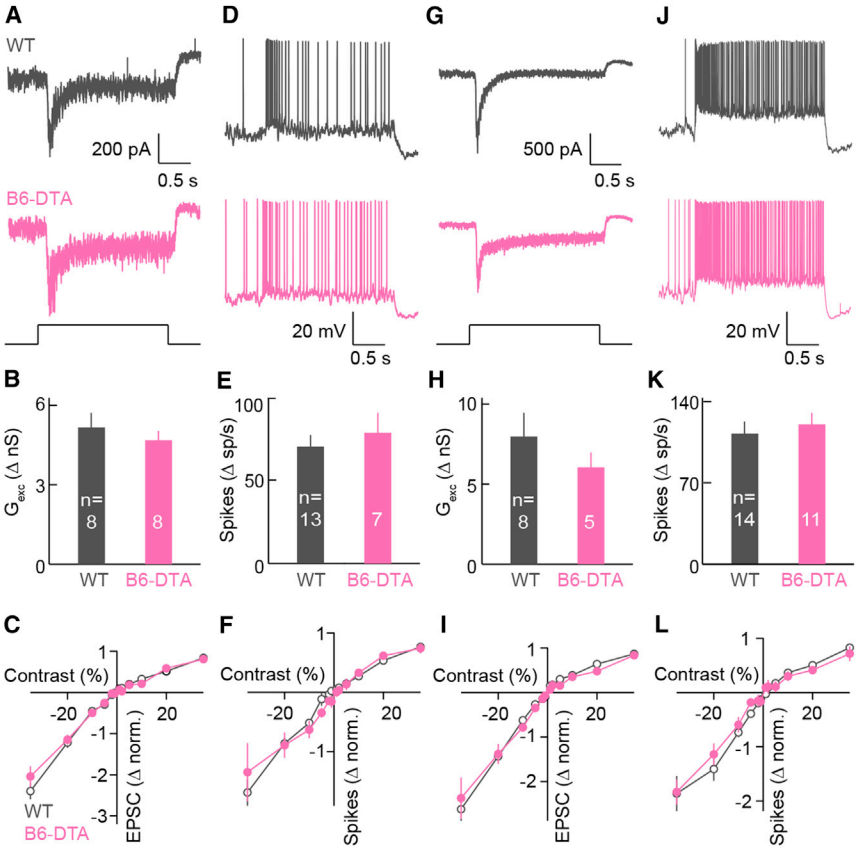

Figure 6. Cell-Type-Specific Rewiring Preserves Contrast Responses of ONα-RGCs in *B6-DTA* Mice

(A and D) Representative EPSC traces (A) and spike responses (D) of ONα-RGCs in wild-type (gray) and *B6-DTA* (pink) mice in illumination conditions preferentially activating rods (mean intensity, 1.5 R*).

(B and E) Summary data of excitatory conductances (B) and spike responses (E) of ONα-RGCs in wild-type (gray) and *B6-DTA* (pink) mice in illumination conditions preferentially activating rods. In (B), WT, 5.16 ± 0.55 nS; *B6-DTA*, 4.69 ± 0.35 nS; p = 0.48. In (E), WT, 70 ± 6.9 sp/s; *B6-DTA*, 78.3 ± 11.9 sp/s; p = 0.56. sp, spikes.

(C and F) Contrast response functions of the normalized excitation (C; WT, n = 11; *B6-DTA*, n = 9) and spike rate (F; WT, n = 12; *B6-DTA*, n = 10).

(G and J) Analogous to (A) and (D) (G and J, respectively), but in conditions preferentially activating cones (mean intensity, 1,500 R*).

(H and K) Analogous to (B) and (E) (H and K, respectively), but in illumination conditions preferentially activating cones. In (H), WT, 7.98 ± 1.48 nS; *B6-DTA*, 6.05 ± 0.92 nS; p = 0.29. In (K), WT, 112.4 ± 10.5 sp/s; *B6-DTA*, 120.4 ± 9.9 sp/s; p = 0.59.

(I and L) Analogous to (C) (I; WT, n = 9; *B6-DTA*, n = 5) and (F) (L; WT, n = 14; *B6-DTA*, n = 8), but in illumination conditions preferentially activating cones.

coincidence of bipolar cell release events. We found that the distributions of sEPSC amplitudes were indistinguishable between wild-type and *B6-DTA* retinas (Figure S5). To explore further possible postsynaptic plasticity, we focally puffed glutamate onto dendrites of ONα-RGCs while recording EPSCs. We included a fluorescent dye (Alexa 488) in the puff solution and used two-photon imaging to measure the application area. These experiments revealed smaller amplitudes of EPSCs per application area in *B6-DTA* mice compared to wild-type littermates (Figure S5). The amplitude reduction (31.6%) matched closely the reduction in synapse density on ONα-RGCs' dendrites (29%) (Figure 3E). Together, these findings exclude broad changes in postsynaptic strength as a major contributor to the response homeostasis and support the notion that, following B6 removal, ONα-RGCs adjust their connectivity with other bipolar cell types in specific ratios to replace the lost input and to precisely preserve their light responses (i.e., circuit-level homeostatic plasticity).

DISCUSSION

During development, most postsynaptic neurons recruit multiple presynaptic partners (i.e., convergence), and by establishing precise numbers of synapses with each partner attain specific function. Whether postsynaptic neurons establish cell-type-specific connectivity patterns with each input independently or balance synapses from different input types to achieve specific function is unclear (Okawa et al., 2014b; Yogev and Shen, 2014). Here, we addressed this question in the convergent innervation of ONα-RGCs by bipolar cells.

Anatomical studies suggested that ONα-RGCs receive input from multiple bipolar cell types, with B6 cells contributing approximately 70% of the excitatory synapses (Morgan et al., 2011; Schwartz et al., 2012; Soto et al., 2012). In our study, optogenetic activation of B6 cells elicited large EPSCs in ONα-RGCs (Figure 1), indicating that functional connectivity in the inner retina matches anatomical connectivity (Morgan and Lichtman, 2013), and that anatomical connectivity was correctly inferred from light microscopic circuit reconstructions (Figures 4 and 5) (Morgan et al., 2011; Schwartz et al., 2012; Soto et al., 2012).

Understanding how signals from the 15 bipolar cell types are distributed and mixed among the 30–40 RGC types is a major challenge in deciphering the functional organization of the retina (Asari and Meister, 2012; Baden et al., 2016; Euler et al., 2014). The results of our pharmacogenetic silencing experiments (Figure 1) indicate that in wild-type mice the light responses of ONα-RGCs are dominated by a single bipolar cell type (B6). These data are consistent with a recent receptive field model, which accurately predicts responses of ONα-RGCs to a variety of stimuli based on their input from B6 cells (Schwartz et al., 2012). Whether dominant input from a single bipolar cell type is the rule or an exception among RGCs remains to be determined (Calkins and Sterling, 2007).

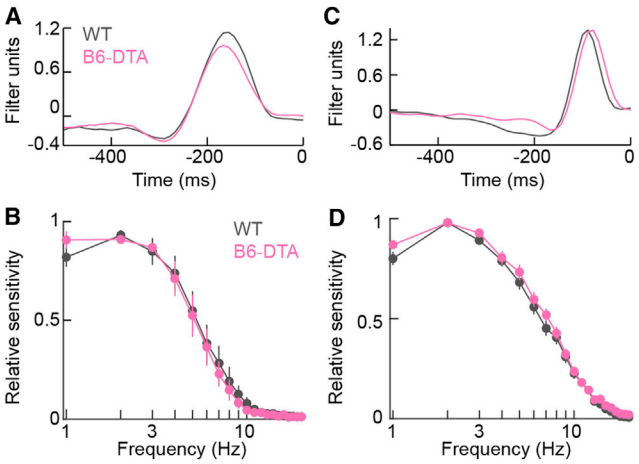

Figure 7. Cell-Type-Specific Rewiring Preserves Temporal Tuning of ONα-RGCs in *B6-DTA* Mice

(A and C) Representative response-weighted stimulus response profiles of excitatory input to ONα-RGCs in conditions preferentially activating rods (A; mean intensity, 1.5 R*) and in conditions preferentially activating cones (C; mean intensity, 1,500 R*) recorded in wild-type (gray) and *B6-DTA* (pink) retinas.

(B and D) Summary data (mean ± SEM) of temporal frequency-response functions computed from Fourier transforms of response-weighted stimulus response profiles in conditions preferentially activating rods (B; WT, n = 9, gray; *B6-DTA*, n = 8, pink) and in conditions preferentially activating cones (D; WT, n = 17, gray; *B6-DTA*, n = 17, pink).

Using an intersectional transgenic strategy (*B6-DTA* mice), we selectively removed B6 cells from the developing retina (Figure 2). In *B6-DTA* mice, ONα-RGCs increased their connectivity with B7 cells, converting this minor input into the major one; formed connections de novo with XBCs (Figures 3 and 4); and maintained synapses from RBCs (Figure 5), which are normally eliminated during circuit maturation (Morgan et al., 2011). Connections of B8 cells with ONα-RGCs were unaffected by B6 removal (Figure 4). Because B8 cells form synapses with ONα-RGCs in wild-type mice, but XBCs do not, the observed rewiring cannot solely reflect competition between bipolar cells. Rewiring reveals that postsynaptic neurons can dynamically adjust connectivity with converging presynaptic inputs rather than forming a fixed number of synapses with each independently. Thus, synaptic specificity in the inner retina is plastic rather than hard-wired. To what extent this is true of other neural circuits remains to be determined (Yogev and Shen, 2014). Interestingly, in the spinal cord, interneurons fail to innervate alternative partners when their primary targets (i.e., sensory fibers) are removed during development (Betley et al., 2009). Differences in the stringency of synaptic specificity may have arisen to limit plasticity to circuits whose function it benefits.

In the retina, as elsewhere in the nervous system, multiple cellular mechanisms are sequentially engaged to establish synaptic specificity (Sanes and Yamagata, 2009; Williams et al., 2010; Yogev and Shen, 2014). Relatively early during development, bipolar cell axons and RGC dendrites stratify in narrow sublaminae of the IPL (Kerschensteiner et al., 2009; Kim et al., 2010; Morgan et al., 2006, 2008). Laminar targeting constrains potential connectivity, differs between cell types, and is determined by a combination of repulsive and adhesive cues (Duan et al., 2014; Matsuoka et al., 2011a, 2011b; Yamagata and Sanes, 2008, 2012). After lamination is complete, connectivity patterns of co-stratifying bipolar cell axons are initially similar, but subsequently diverge through cell-type-specific changes in the conversion of axo-dendritic contacts into synapses (i.e., connectivity fraction) (Morgan et al., 2011). We find that plasticity elicited by B6 removal selectively engages this mechanism. The morphologies of bipolar cell axons and ONα-RGC dendrites, and the numbers of contacts between them, are unchanged in *B6-DTA* compared to wild-type mice, but the connectivity fractions of axo-dendritic contacts are altered in a cell-type-specific manner (Figures 3, 4, and 5). Because bipolar cell types with similar responses show overlapping axonal stratification patterns (Baden et al., 2013; Borghuis et al., 2013; Euler et al., 2014; Franke et al., 2017), rewiring within a constant laminar position may best allow ONα-RGCs to regain their specific function. Even within a constant laminar position, however, ONα-RGCs make distinct choices in normal development (Morgan et al., 2011) and in plasticity (e.g., not to increase connectivity with B8). Furthermore, it is worth noting that the laminar constraint on rewiring is not absolute. Thus, when several ON cone bipolar cell types as well as RBCs are removed during development, ONα-RGCs extend dendritic arbors into outer IPL and recruit input from OFF cone bipolar cells (Okawa et al., 2014a).

Homeostatic plasticity had previously been shown to stabilize average firing rates (Hengen et al., 2013; Turrigiano and Nelson, 2004) and spontaneous activity patterns of neurons (Blankenship and Feller, 2010; Kerschensteiner, 2014), but how it regulates their unique circuit functions remained unclear. In assessing the functional consequences of plasticity in *B6-DTA* mice, we find that it not only rescues overall activity levels of ONα-RGCs, but indeed also precisely restores their contrast (Figure 6) and temporal response properties (Figure 7), both of which RGCs inherit from their combined bipolar cell inputs. Our sEPSC recordings and glutamate puff experiments suggest that postsynaptic scaling does not play a major role in this response preservation (Figure S5). Instead, homeostatic plasticity controls cell-type-specific wiring of presynaptic inputs (i.e., bipolar cells), expanding its reach beyond the intrinsic and synaptic mechanisms previously characterized at the level of individual neurons (Pozo and Goda, 2010; Turrigiano, 2008; Wefelmeyer et al., 2016). In this way, circuit-level homeostatic plasticity shapes cell-type-specific wiring in the inner retina and stabilizes visual information sent to the brain.

STAR★METHODS

Detailed methods are provided in the online version of this paper and include the following:

- KEY RESOURCES TABLE
- CONTACT FOR REAGENT AND RESOURCE SHARING
- EXPERIMENTAL MODEL AND SUBJECT DETAILS
  - Mice

SUPPLEMENTAL INFORMATION

Supplemental Information includes five figures and can be found with this article online at http://dx.doi.org/10.1016/j.neuron.2017.04.016.

AUTHOR CONTRIBUTIONS

N.-W.T. and D.K. designed this study. N.-W.T. performed and analyzed the experiments. F.S. provided reagents. N.-W.T. and D.K. wrote software and the manuscript with input from F.S.

ACKNOWLEDGMENTS

We thank members of the Kerschensteiner lab for helpful comments and suggestions throughout this study, and Lei Zhao for expert technical assistance. We are grateful to Dr. Peter Lukasiewicz for lending us equipment for puff experiments. We thank Dr. Mae Gordon and her team for advice on statistics. This work was supported by the NIH (EY023341 and EY026978 to D.K. and Vision Core Grant EY0268) and the Research to Prevent Blindness Foundation (Career Development Award to D.K., and an unrestricted grant to the Department of Ophthalmology and Visual Sciences at Washington University).

Received: November 29, 2016
Revised: March 17, 2017
Accepted: April 11, 2017
Published: April 27, 2017

REFERENCES

Akrouh, A., and Kerschensteiner, D. (2013). Intersecting circuits generate precisely patterned retinal waves. Neuron *79*, 322–334.

Antonini, A., and Stryker, M.P. (1993). Rapid remodeling of axonal arbors in the visual cortex. Science *260*, 1819–1821.

Asari, H., and Meister, M. (2012). Divergence of visual channels in the inner retina. Nat. Neurosci. *15*, 1581–1589.

Baden, T., Berens, P., Bethge, M., and Euler, T. (2013). Spikes in mammalian bipolar cells support temporal layering of the inner retina. Curr. Biol. *23*, 48–52.

Baden, T., Berens, P., Franke, K., Román Rosón, M., Bethge, M., and Euler, T. (2016). The functional diversity of retinal ganglion cells in the mouse. Nature *529*, 345–350.

Betley, J.N., Wright, C.V., Kawaguchi, Y., Erdélyi, F., Szabó, G., Jessell, T.M., and Kaltschmidt, J.A. (2009). Stringent specificity in the construction of a GABAergic presynaptic inhibitory circuit. Cell *139*, 161–174.

Blankenship, A.G., and Feller, M.B. (2010). Mechanisms underlying spontaneous patterned activity in developing neural circuits. Nat. Rev. Neurosci. *11*, 18–29.

Bloomfield, S.A., and Dacheux, R.F. (2001). Rod vision: pathways and processing in the mammalian retina. Prog. Retin. Eye Res. *20*, 351–384.

Borghuis, B.G., Marvin, J.S., Looger, L.L., and Demb, J.B. (2013). Two-photon imaging of nonlinear glutamate release dynamics at bipolar cell synapses in the mouse retina. J. Neurosci. *33*, 10972–10985.

Calkins, D.J., and Sterling, P. (2007). Microcircuitry for two types of achromatic ganglion cell in primate fovea. J. Neurosci. *27*, 2646–2653.

Davis, G.W., and Müller, M. (2015). Homeostatic control of presynaptic neurotransmitter release. Annu. Rev. Physiol. *77*, 251–270.

Demb, J.B., and Singer, J.H. (2015). Functional circuitry of the retina. Annual Review of Vision Science *1*, 263–289.

Duan, X., Krishnaswamy, A., De la Huerta, I., and Sanes, J.R. (2014). Type II cadherins guide assembly of a direction-selective retinal circuit. Cell *158*, 793–807.

Dunn, F.A., and Wong, R.O. (2012). Diverse strategies engaged in establishing stereotypic wiring patterns among neurons sharing a common input at the visual system's first synapse. J. Neurosci. *32*, 10306–10317.

Dunn, F.A., and Wong, R.O. (2014). Wiring patterns in the mouse retina: collecting evidence across the connectome, physiology and light microscopy. J. Physiol. *592*, 4809–4823.

Ebert, D.H., and Greenberg, M.E. (2013). Activity-dependent neuronal signalling and autism spectrum disorder. Nature *493*, 327–337.

Euler, T., Haverkamp, S., Schubert, T., and Baden, T. (2014). Retinal bipolar cells: elementary building blocks of vision. Nat. Rev. Neurosci. *15*, 507–519.

Fisher, L.J. (1979). Development of synaptic arrays in the inner plexiform layer of neonatal mouse retina. J. Comp. Neurol. *187*, 359–372.

Fox, M.A., and Sanes, J.R. (2007). Synaptotagmin I and II are present in distinct subsets of central synapses. J. Comp. Neurol. *503*, 280–296.

Franke, K., Berens, P., Schubert, T., Bethge, M., Euler, T., and Baden, T. (2017). Inhibition decorrelates visual feature representations in the inner retina. Nature *542*, 439–444.

Grimes, W.N., Schwartz, G.W., and Rieke, F. (2014). The synaptic and circuit mechanisms underlying a change in spatial encoding in the retina. Neuron *82*, 460–473.

Grimm, D., Kay, M.A., and Kleinschmidt, J.A. (2003). Helper virus-free, optically controllable, and two-plasmid-based production of adeno-associated virus vectors of serotypes 1 to 6. Mol. Ther. *7*, 839–850.

Helmstaedter, M., Briggman, K.L., Turaga, S.C., Jain, V., Seung, H.S., and Denk, W. (2013). Connectomic reconstruction of the inner plexiform layer in the mouse retina. Nature *500*, 168–174.

Hengen, K.B., Lambo, M.E., Van Hooser, S.D., Katz, D.B., and Turrigiano, G.G. (2013). Firing rate homeostasis in visual cortex of freely behaving rodents. Neuron *80*, 335–342.

Ichinose, T., Fyk-Kolodziej, B., and Cohn, J. (2014). Roles of ON cone bipolar cell subtypes in temporal coding in the mouse retina. J. Neurosci. *34*, 8761–8771.

Kerschensteiner, D. (2014). Spontaneous network activity and synaptic development. Neuroscientist *20*, 272–290.

Kerschensteiner, D., Morgan, J.L., Parker, E.D., Lewis, R.M., and Wong, R.O. (2009). Neurotransmission selectively regulates synapse formation in parallel circuits in vivo. Nature *460*, 1016–1020.

Kim, I.J., Zhang, Y., Meister, M., and Sanes, J.R. (2010). Laminar restriction of retinal ganglion cell dendrites and axons: subtype-specific developmental patterns revealed with transgenic markers. J. Neurosci. *30*, 1452–1462.

Kim, T., Soto, F., and Kerschensteiner, D. (2015). An excitatory amacrine cell detects object motion and provides feature-selective input to ganglion cells in the mouse retina. eLife *4*, http://dx.doi.org/10.7554/eLife.08025.

Klugmann, M., Symes, C.W., Leichtlein, C.B., Klaussner, B.K., Dunning, J., Fong, D., Young, D., and During, M.J. (2005). AAV-mediated hippocampal expression of short and long Homer 1 proteins differentially affect cognition and seizure activity in adult rats. Mol. Cell. Neurosci. *28*, 347–360.

Lagali, P.S., Balya, D., Awatramani, G.B., Münch, T.A., Kim, D.S., Busskamp, V., Cepko, C.L., and Roska, B. (2008). Light-activated channels targeted to ON

bipolar cells restore visual function in retinal degeneration. Nat. Neurosci. *11*, 667–675.

Madisen, L., Zwingman, T.A., Sunkin, S.M., Oh, S.W., Zariwala, H.A., Gu, H., Ng, L.L., Palmiter, R.D., Hawrylycz, M.J., Jones, A.R., et al. (2010). A robust and high-throughput Cre reporting and characterization system for the whole mouse brain. Nat. Neurosci. *13*, 133–140.

Madisen, L., Mao, T., Koch, H., Zhuo, J.M., Berenyi, A., Fujisawa, S., Hsu, Y.W., Garcia, A.J., 3rd, Gu, X., Zanella, S., et al. (2012). A toolbox of Cre-dependent optogenetic transgenic mice for light-induced activation and silencing. Nat. Neurosci. *15*, 793–802.

Magnus, C.J., Lee, P.H., Atasoy, D., Su, H.H., Looger, L.L., and Sternson, S.M. (2011). Chemical and genetic engineering of selective ion channel-ligand interactions. Science *333*, 1292–1296.

Matsuoka, R.L., Chivatakarn, O., Badea, T.C., Samuels, I.S., Cahill, H., Katayama, K., Kumar, S.R., Suto, F., Chédotal, A., Peachey, N.S., et al. (2011a). Class 5 transmembrane semaphorins control selective Mammalian retinal lamination and function. Neuron *71*, 460–473.

Matsuoka, R.L., Nguyen-Ba-Charvet, K.T., Parray, A., Badea, T.C., Chédotal, A., and Kolodkin, A.L. (2011b). Transmembrane semaphorin signalling controls laminar stratification in the mammalian retina. Nature *470*, 259–263.

Morgan, J.L., and Lichtman, J.W. (2013). Why not connectomics? Nat. Methods *10*, 494–500.

Morgan, J.L., Dhingra, A., Vardi, N., and Wong, R.O. (2006). Axons and dendrites originate from neuroepithelial-like processes of retinal bipolar cells. Nat. Neurosci. *9*, 85–92.

Morgan, J.L., Schubert, T., and Wong, R.O. (2008). Developmental patterning of glutamatergic synapses onto retinal ganglion cells. Neural Dev. *3*, 8.

Morgan, J.L., Soto, F., Wong, R.O., and Kerschensteiner, D. (2011). Development of cell type-specific connectivity patterns of converging excitatory axons in the retina. Neuron *71*, 1014–1021.

Murphy, G.J., and Rieke, F. (2006). Network variability limits stimulus-evoked spike timing precision in retinal ganglion cells. Neuron *52*, 511–524.

Okawa, H., Della Santina, L., Schwartz, G.W., Rieke, F., and Wong, R.O. (2014a). Interplay of cell-autonomous and nonautonomous mechanisms tailors synaptic connectivity of converging axons in vivo. Neuron *82*, 125–137.

Okawa, H., Hoon, M., Yoshimatsu, T., Della Santina, L., and Wong, R.O. (2014b). Illuminating the multifaceted roles of neurotransmission in shaping neuronal circuitry. Neuron *83*, 1303–1318.

Pozo, K., and Goda, Y. (2010). Unraveling mechanisms of homeostatic synaptic plasticity. Neuron *66*, 337–351.

Purves, D., and Lichtman, J.W. (1980). Elimination of synapses in the developing nervous system. Science *210*, 153–157.

Ramocki, M.B., and Zoghbi, H.Y. (2008). Failure of neuronal homeostasis results in common neuropsychiatric phenotypes. Nature *455*, 912–918.

Riccomagno, M.M., and Kolodkin, A.L. (2015). Sculpting neural circuits by axon and dendrite pruning. Annu. Rev. Cell Dev. Biol. *31*, 779–805.

Sanes, J.R., and Yamagata, M. (2009). Many paths to synaptic specificity. Annu. Rev. Cell Dev. Biol. *25*, 161–195.

Schindelin, J., Arganda-Carreras, I., Frise, E., Kaynig, V., Longair, M., Pietzsch, T., Preibisch, S., Rueden, C., Saalfeld, S., Schmid, B., et al. (2012). Fiji: an open-source platform for biological-image analysis. Nat. Methods *9*, 676–682.

Schmitz, F., Königstorfer, A., and Südhof, T.C. (2000). RIBEYE, a component of synaptic ribbons: a protein's journey through evolution provides insight into synaptic ribbon function. Neuron *28*, 857–872.

Schwartz, G.W., Okawa, H., Dunn, F.A., Morgan, J.L., Kerschensteiner, D., Wong, R.O., and Rieke, F. (2012). The spatial structure of a nonlinear receptive field. Nat. Neurosci. *15*, 1572–1580.

Shekhar, K., Lapan, S.W., Whitney, I.E., Tran, N.M., Macosko, E.Z., Kowalczyk, M., Adiconis, X., Levin, J.Z., Nemesh, J., Goldman, M., et al. (2016). Comprehensive classification of retinal bipolar neurons by single-cell transcriptomics. Cell *166*, 1308–1323.e30.

Soto, F., Ma, X., Cecil, J.L., Vo, B.Q., Culican, S.M., and Kerschensteiner, D. (2012). Spontaneous activity promotes synapse formation in a cell-type-dependent manner in the developing retina. J. Neurosci. *32*, 5426–5439.

Taniguchi, H., He, M., Wu, P., Kim, S., Paik, R., Sugino, K., Kvitsiani, D., Fu, Y., Lu, J., Lin, Y., et al. (2011). A resource of Cre driver lines for genetic targeting of GABAergic neurons in cerebral cortex. Neuron *71*, 995–1013.

Tien, N.W., Pearson, J.T., Heller, C.R., Demas, J., and Kerschensteiner, D. (2015). Genetically identified suppressed-by-contrast retinal ganglion cells reliably signal self-generated visual stimuli. J. Neurosci. *35*, 10815–10820.

Tien, N.W., Kim, T., and Kerschensteiner, D. (2016). Target-specific glycinergic transmission from VGluT3-expressing amacrine cells shapes suppressive contrast responses in the retina. Cell Rep. *15*, 1369–1375.

Turrigiano, G.G. (2008). The self-tuning neuron: synaptic scaling of excitatory synapses. Cell *135*, 422–435.

Turrigiano, G.G., and Nelson, S.B. (2004). Homeostatic plasticity in the developing nervous system. Nat. Rev. Neurosci. *5*, 97–107.

Ueda, Y., Iwakabe, H., Masu, M., Suzuki, M., and Nakanishi, S. (1997). The mGluR6 5′ upstream transgene sequence directs a cell-specific and developmentally regulated expression in retinal rod and ON-type cone bipolar cells. J. Neurosci. *17*, 3014–3023.

Wang, Y.V., Weick, M., and Demb, J.B. (2011). Spectral and temporal sensitivity of cone-mediated responses in mouse retinal ganglion cells. J. Neurosci. *31*, 7670–7681.

Wässle, H., Puller, C., Müller, F., and Haverkamp, S. (2009). Cone contacts, mosaics, and territories of bipolar cells in the mouse retina. J. Neurosci. *29*, 106–117.

Wefelmeyer, W., Puhl, C.J., and Burrone, J. (2016). Homeostatic plasticity of subcellular neuronal structures: from inputs to outputs. Trends Neurosci. *39*, 656–667.

Williams, M.E., de Wit, J., and Ghosh, A. (2010). Molecular mechanisms of synaptic specificity in developing neural circuits. Neuron *68*, 9–18.

Yamagata, M., and Sanes, J.R. (2008). Dscam and Sidekick proteins direct lamina-specific synaptic connections in vertebrate retina. Nature *451*, 465–469.

Yamagata, M., and Sanes, J.R. (2012). Expanding the Ig superfamily code for laminar specificity in retina: expression and role of contactins. J. Neurosci. *32*, 14402–14414.

Yogev, S., and Shen, K. (2014). Cellular and molecular mechanisms of synaptic specificity. Annu. Rev. Cell Dev. Biol. *30*, 417–437.

Yu, C.R., Power, J., Barnea, G., O'Donnell, S., Brown, H.E., Osborne, J., Axel, R., and Gogos, J.A. (2004). Spontaneous neural activity is required for the establishment and maintenance of the olfactory sensory map. Neuron *42*, 553–566.

Zaghloul, K.A., Boahen, K., and Demb, J.B. (2003). Different circuits for ON and OFF retinal ganglion cells cause different contrast sensitivities. J. Neurosci. *23*, 2645–2654.

Zhu, Y., Xu, J., Hauswirth, W.W., and DeVries, S.H. (2014). Genetically targeted binary labeling of retinal neurons. J. Neurosci. *34*, 7845–7861.

STAR★METHODS

KEY RESOURCES TABLE

REAGENT or RESOURCE	SOURCE	IDENTIFIER
Antibodies		
Mouse monoclonal anti-synaptotagmin II	Zebrafish International Resource Center	Cat# znp-1; RRID: AB_10013783
Rabbit polyclonal anti-DsRed	Clontech Laboratories	Cat# 632496; RRID: AB_10013483
Guinea pig polyclonal anti-VGLUT1	Millipore	Cat# AB5905; RRID: AB_2301751
Mouse monoclonal anti-CtBP2	BD Biosciences	Cat# 612044; RRID: AB_399431
Chicken polyclonal anti-GFP	Thermo Fisher Scientific	Cat# A10262; RRID: AB_2534023
Goat polyclonal anti-mouse, Alexa Fluor 633	Thermo Fisher Scientific	Cat# A-21050; RRID: AB_2535718
Goat polyclonal anti-rabbit, Alexa Fluor 568	Thermo Fisher Scientific	Cat# A-11011; RRID: AB_143157
Goat polyclonal anti-mouse, Alexa Fluor 568	Thermo Fisher Scientific	Cat# A-11004; RRID: AB_2534072
Donkey polyclonal anti-chicken IgY, Alexa Fluor 488	Jackson ImmunoResearch Labs	Cat# 703-545-155; RRID: AB_2340375
Bacterial and Virus Strains		
pAAV-Grm6s-tdT	This paper	N/A
pAAV-Grm6s-FLEX-rev-PSAM$^{L141F,\ Y115F}$-GlyR-IRES-GFP	This paper	N/A
Chemicals, Peptides, and Recombinant Proteins		
Normal Donkey Serum	Sigma-Aldrich	Cat# D9663
Alexa Fluor 488 hydrazide, sodium salt	Thermo Fisher Scientific	Cat# A10436
Alexa Fluor 568 hydrazide, sodium salt	Thermo Fisher Scientific	Cat# A10437
L-AP4	Tocris	Cat# 0103
ACET	Tocris	Cat# 2728
HEX	Sigma-Aldrich	Cat# H0879
NBQX	Tocirs	Cat# 1044
D-AP5	Tocris	Cat# 0106
PSEM^{308}	Apex Scientific	N/A
Meclofenamic acid (MFA)	Sigma-Aldrich	Cat# M4531
Vectashield	Vector Laboratories	Cat# H-1000
Experimental Models: Organisms/Strains		
Mouse model: CCK-ires-Cre	The Jackson Laboratory	Strain: #012706
Mouse model: Ai9	The Jackson Laboratory	Strain: #007905
Mouse model: Ai32	The Jackson Laboratory	Strain: #012569
Mouse model: Grm6$_L$-YFP-DTA^{con}	(Morgan et al., 2011)	N/A
Mouse model: B6-DTA	This paper	N/A
Recombinant DNA		
Plasmid: CAG::PSAM^{L141F,Y115F}:GlyR-IRES-GFP	Addgene	Cat# 32480
Software and Algorithms		
Fiji	NIH	https://imagej.nih.gov/ij/
MATLAB	MathWorks	https://www.mathworks.com/products/matlab.html
Mini Analysis Program	Synaptosoft	http://www.synaptosoft.com/MiniAnalysis/
Amira	FEI Imaging	https://www.fei.com/software/amira-for-life-sciences/

CONTACT FOR REAGENT AND RESOURCE SHARING

Further information and requests for reagents should be directed to and will be fulfilled by the Lead Contact, Daniel Kerschensteiner (kerschensteinerd@wustl.edu).

EXPERIMENTAL MODEL AND SUBJECT DETAILS

Mice

Throughout this study, we used *CCK-ires-Cre* (Taniguchi et al., 2011) mice (i) crossed to a tdTomato reporter strain (*Ai9*) (Madisen et al., 2010), (ii) crossed to a channelrhodopsin-2 reporter strain (*Ai32*) (Madisen et al., 2012), (iii) crossed to mice in which a 9 kb fragment of the *Grm6* promoter (i.e., $Grm6_L$) (Ueda et al., 1997) drives expression of YFP or, upon Cre-mediated recombination, of an attenuated version of diphtheria toxin $Grm6_L$-*YFP-DTA*^{con} (Morgan et al., 2011), or (iv) injected with AAVs. For our experiments, we isolated retinas from young adult (postnatal day 20-40) mice of both sexes. All procedures were approved by the Animal Studies Committee of Washington University School of Medicine and performed in compliance with the National Institutes of Health Guide for the Care and Use of Laboratory Animals.

METHOD DETAILS

Adeno-associated viruses

To label ON cone bipolar and rod bipolar cells, we generated adeno-associated viruses (AAVs) in which four concatenated repeats of a 200 bp fragment of the *Grm6* promoter ($Grm6_S$) (Lagali et al., 2008) drive expression of tdTomato, a red fluorescent protein (plasmid: *pAAV-*$Grm6_S$*-tdT*). The *pAAV-*$Grm6_S$*-PSAM*^{con} vector for pharmacogenetic silencing was derived by replacing tdTomato sequences of *pAAV-*$Grm6_S$*-tdT* with a *FLEX-rev-PSAM*$^{L141F,\ Y115F}$*-GlyR-IRES-GFP* cassette (Addgene plasmid: 32480) (Magnus et al., 2011). The *pAAV-*$Grm6_s$*-GFP*^{con} plasmid was generated by removing PSAM-IRES sequences from *pAAV-*$Grm6_S$*-PSAM*^{con}. Viral particles were packaged and purified as previously described (Grimm et al., 2003; Klugmann et al., 2005). Briefly, AAV1/2 chimeric virions were produced by co-transfecting HEK293 cells with *pAAV-*$Grm6_S$*-tdT*, *pAAV-*$Grm6_S$*-PSAM*^{con} or *pAAV-*$Grm6_s$*-GFP*^{con}, and helper plasmids encoding Rep2 and the Cap for serotype 1 and Rep2 and the Cap for serotype 2. Forty-eight hours after transfection, cells and supernatant were harvested and viral particles purified using heparin affinity columns (Sigma). Viruses (250 nL) were injected with a NanojectII (Drummond) into the vitreous chamber of newborn mice anesthetized on ice.

Tissue preparation

Mice were euthanized with CO_2 followed by decapitation and enucleation. For imaging, eyes were transferred into oxygenated mouse artificial cerebrospinal fluid ($mACSF_{HEPES}$) containing (in mM): 119 NaCl, 2.5 KCl, 1 NaH_2PO_4, 2.5 $CaCl_2$, 1.3 $MgCl_2$, 20 HEPES, and 11 glucose (pH adjusted to 7.37 using NaOH). Retinas were either isolated and mounted flat on filter paper, or left in the eyecup for 30 min fixation with 4% paraformaldehyde in $mACSF_{HEPES}$ (Tien et al., 2016). For patch clamp recordings, mice were dark adapted at least 2 hr before their retinas were isolated under infrared illumination (> 900 nm) in oxygenated $mACSF_{NaHCO3}$ containing (in mM) 125 NaCl, 2.5 KCl, 1 $MgCl_2$, 1.25 NaH_2PO_4, 2 $CaCl_2$, 20 glucose, 26 $NaHCO_3$ and 0.5 L-glutamine equilibrated with 95% O_2 / 5% CO_2 (Tien et al., 2016).

Immunohistochemistry

After blocking for 2 hr with 5% Normal Donkey Serum in PBS, vibratome slices (60 μm in thickness) embedded in 4% agarose (Sigma) were incubated overnight at 4°C with primary antibodies. Slices were then washed in PBS (3 × 20 min) and incubated in secondary antibodies for 2 hr at room temperature. Flat-mount preparations were frozen and thawed three times after cryoprotection (1 hr 10% sucrose in PBS at RT, 1 hr 20% sucrose in PBS at RT, and overnight 30% sucrose in PBS at 4°C), blocked with 5% Normal Donkey Serum in PBS for 2 hr, and then incubated with primary antibodies for 5 d at 4°C and washed in PBS (3 × 1 hr) at RT. Subsequently, flat mounts were incubated with secondary antibodies for 1 d at 4°C and washed in PBS (3 × 1 hr) at room temperature. The following primary antibodies were used in this study: mouse anti-synaptotagmin II (znp-1, 1:500, Zebrafish International Resource Center), rabbit anti-tdTomato (1:1000, Clontech Laboratories), guinea pig anti-VGluT1 (1:500, Millipore), chicken anti-GFP (1:500, thermos Fisher Scientific) and mouse anti-CtBP2 (1:500, BD Biosciences). Secondary antibodies were Alexa 568- and Alexa 633 conjugates (1:1000, Invitrogen).

Electrophysiology

Cell-attached and whole-cell patch clamp recordings were obtained in the dorsal halves (Wang et al., 2011) of dark-adapted flat-mounted retinas superfused (5-7 mL / min) with warm (30-33°C) $mACSF_{NaHCO3}$ as previously described (Tien et al., 2016). ONα-RGCs were selected under infrared illumination based on their large soma size (diameter > 20 μm); and correct targeting was confirmed by inclusion of Alexa 488 or Alexa 568 (0.1 mM) in the intracellular solution and 2-photon imaging at the end of each recording. The intracellular solution for current-clamp recordings contained (in mM) 125 K-gluconate, 10 NaCl, 1 $MgCl_2$, 10 EGTA, 5 HEPES, 5 ATP-Na_2, and 0.1 GTP-Na (pH adjusted to 7.2 with KOH). The intracellular solution voltage-clamp recordings contained (in mM)

120 Cs-gluconate, 1 $CaCl_2$, 1 $MgCl_2$, 10 Na-HEPES, 11 EGTA, 10 TEA-Cl, 2 Qx314, ATP-Na_2, and 0.1 GTP-Na (pH adjusted to 7.2 with CsOH). Patch pipettes had resistances of 3-6 MΩ (borosilicate glass). Liquid junction potentials were corrected offline. Signals were amplified with a Multiclamp 700B amplifier (Molecular Devices), filtered at 3 kHz (8-pole Bessel low-pass), and sampled at 10 kHz (Digidata 1440A, Molecular Devices). Excitatory postsynaptic currents (EPSCs) were measured at the reversal potential of inhibitory (−60 mV) conductances. For optogenetic experiments, the following reagents were applied individually or in combinations: L-AP4 (20 μM, Tocris), ACET (10 μM, Tocris), HEX (300 μM, Tocris), D-AP5 (30 μM, Tocris) and NBQX (40 μM, Tocris). For pharmacogenetic silencing, $PSEM^{308}$ (20 μM, Apex Scientific) was bath-applied for at least 15 min. Meclofenamic acid (MFA, 200 μM, Sigma) was used to block gap junctions. To isolate the spontaneous excitatory synaptic currents (sEPSCs), the tissue was bathed in $mACSF_{NaHCO3}$ with zero calcium concentration to block neurotransmission. In puff experiments, glutamate (1 mM in $mACSF_{NaHCO3}$, Sigma) was focally applied near the primary dendrites of ONα-RGCs by delivering pressure (5 psi) to a patch pipette via a Picospritzer II (Parker Hannifin). Alexa 488 (0.1 mM) was included in the puff solution to estimate the application area under two-photon imaging (Akrouh and Kerschensteiner, 2013). Two to three primary dendrites were tested per cell, and five to six puffs of glutamate of various durations (5-100 ms) were applied to the same location.

Light stimulation

For optogenetic experiments, light from a mercury bulb (Olympus) was band-pass filtered (426-446 nm, Chroma) and focused onto RGC side of the retina (intensity: 3.15×10^{-4} W / mm^2) through a 20 × 0.95 NA water immersion objective. Stimulus timing was controlled by a Uniblitz shutter (Vincent Associates). To probe photoreceptor-mediated light responses, stimuli were written in MATLAB (MathWorks), presented on an organic light-emitting display (eMagin; refresh rate, 60 Hz) using Cogent graphics extensions (John Romaya, University College London, London, UK), and focused onto the photoreceptor side of the retina via a substage condenser. Stimuli were centered on the soma of the recorded cell with mean intensity of either 1.5 or 1500 rhodopsin isomerization / rod / s (R*). To test contrast sensitivity, short luminance steps (250 ms) were presented every 2.25 s in a circular area (diameter: 300 μm). To probe spatiotemporal tuning, the stimulus display was divided into vertical bars (width: 50 μm, height: 600 μm), and the intensity of each bar randomly updated from a Gaussian distribution every 33 ms (refresh rate: 30 Hz) for 15 min.

Biolistic transfection

Gold particles (1.6 μm diameter, Bio-Rad) were coated with plasmids encoding cytosolic tdTomato or YFP under the cytomegalovirus promoter, and postsynaptic density protein 95 (PSD95) fused at its C terminus to CFP (Morgan et al., 2011). We used a helium-pressurized gun (40 psi, Bio-Rad) to deliver particles to RGCs and incubated the transfected retinas into $mACSF_{HEPES}$ in a humid oxygenated chamber at 33°C for 16-18 hr.

Imaging

Images were acquired on an Fv1000 confocal microscope (Olympus) using a 20 × 0.85 NA or 60 × 1.35 NA oil immersion objective. Image stacks of ONα-RGC dendrites and synapse patterns were acquired at a voxel size 0.103-0.3 μm (x/y-z axis). Bipolar cell image stacks were acquired at a voxel size range of 0.11, 0.082 or 0.066 μm-0.3 μm (x/y-z axis). Bipolar cell types were identified by their characteristic axonal and dendritic morphology (Dunn and Wong, 2012; Helmstaedter et al., 2013; Kerschensteiner et al., 2009; Morgan et al., 2011).

QUANTIFICATION AND STATISTICAL ANALYSIS

Electrophysiology analysis

For contrast steps as well as optogenetic stimulation, baseline-subtracted averaged responses (spike rate or conductance) were measured during 100-200 ms time windows. Temporal response profiles were calculated by reverse correlation of the stimulus with the response and averaged for stimulus bars overlaying the receptive field center (i.e., response-weighted stimulus averages) (Kim et al., 2015). Frequency tuning was then computed by Fourier transforms of the temporal response profiles. All analyses above were performed using custom scripts written in MATLAB. Area and amplitude thresholds (Mini Analysis, Synaptosoft) were optimized to detect sEPSC events in each recording (Kerschensteiner et al., 2009). sEPSCs traces presented in the figures were additionally low-pass filtered at 2 kHz for display. For puff experiments, baseline-subtracted averaged responses (conductance) were normalized by the application area measured by 2-photon imaging of the Alexa 488 included in the puff solution.

Imaging Analysis

ONα-RGC dendrites and synapse patterns were reconstructed from image stacks using local thresholding in Amira (FEI Imaging) and previously described custom software written in MATLAB (Kerschensteiner et al., 2009; Morgan et al., 2008). For the stratification calculation, dendrites were skeletonized into segments of ~0.5 μm length. For each segment, the distance of its z-position to the median z-position of all segments within a 30-μm radius was computed, and this measure averaged across all segments of a cell to quantify its stratification. Use of a 30-μm radius prevents broader distortions of the tissue from influencing measurements of stratification. Dendritic skeletonization and stratification analysis was performed using custom scripts written in MATLAB (Morgan et al., 2011). Colocalization of PSD95 puncta and CtBP2 puncta was assessed visually in Fiji (Schindelin et al., 2012). The connectivity

of pairs of bipolar cells and ONα-RGCs was analyzed in image stacks as previously described (Morgan et al., 2011). Briefly, dendrites of ONα-RGCs and axons of bipolar cells were masked in 3D using local thresholding in Amira. Contacts were defined as points of overlap between axon and dendrite masks exceeding 50 connected voxels; and synapses counted when PSD95 puncta were found within such a volume of axon-dendrite overlap. Bipolar cell axon territories were measured by the area of the smallest convex polygons encompassing their arbors in a maximum intensity projection.

Statistics

Paired and unpaired t tests were used to assess the statistical significance of differences between single parameter characteristics (e.g., dendrite length) of experimental groups. Cumulative probabilities of sEPSCs amplitudes, Contrast- and temporal frequency response functions of *B6-DTA* mice and wild-type littermates (or before, during and after PSEM^{308} application) were compared using bootstrapping with 10,000 replicates. Differences in the average response curves of *B6-DTA* and wild-type mice were compared to differences generated by random assignments of data to the two genotypes (confidence interval: 95%). For all figures significance corresponds to *$p < 0.05$, **$p < 0.01$, ***$p < 0.001$, ****$p < 0.0001$ for the comparisons indicated in the figure or figure legend.